Chapter 4

Effect of Ni incorporation in $KCoPO_4$ on the charge storage capacity of $KCo_{1-x}Ni_xPO_4$ ($0 \leq x \leq 0.5$) Electrodes for the Fabrication of High-Performing Hybrid Supercapacitors

4.1 Introduction

Rising global energy demand has been primarily satisfied through the combustion of fossil fuels in an effort to sustain economic growth and development. This, however, has led to an increased greenhouse gas emission into the atmosphere, thus accelerating global warming and environmental degradation. A change in energy source toward cleaner and more sustainable energy sources is needed. Renewable energy sources such as solar, wind, and tidal power have come out in the limelight for filling the energy demands of this world in a much environment-friendly way. [1]-[3] These renewable sources are vast and sustainable, which will even reduce carbon emissions considerably in the future.

But among some of the major drawbacks associated with these renewable energy technologies is that they appear to be intermittent in nature. The generation of energy from natural sources such as solar or wind is completely dependent upon the weather and time conditions, as well as by geographical location. This type of power generation may cause constant fluctuations in energy output, which serves as a constraint in ascertaining constant and un-interrupted supply. In cases of large-scale applications, efficient methods of energy storage systems need to ensure that energy should be drawn at the required time. Large-scale electrochemical energy conversion and storage devices, such as batteries and Supercapacitors, play a critical role in the integration of renewable energy into the power grid and energy stability. [3–8]

Batteries and Supercapacitors have received great attention lately because of their capability to store and release energy. High power efficiency and high energy storage capacity along with excellent cycling stabilities under the condition of fast charge-discharge performance rate qualify them for the category. Batteries, for example are known to possess a strong aspect of energy density which offers this enormous energy storage. Energy storing will be via diffusion

of the ionic movement that will subsequently take place through redox in bulk of the electrode materials. The sluggish nature of the faradaic (redox) charge storage process, however, leads to low power density in batteries despite high energy density. This leads to a low ability to supply power for applications requiring high power output.

On the other hand, Supercapacitors store energy through a physical process known as electrostatic adsorption. Electrolyte ions are adsorbed onto the surface of the electrode material, which leads to a double-layer charge storage mechanism. This enables Supercapacitors to deliver significantly higher power densities and achieve rapid charge-discharge cycles compared to batteries. However, their primary limitation lies in their relatively low energy density, as the charge storage is limited to the electrode surface area. [5]

In an effort to overcome the drawbacks of both batteries and Supercapacitors, scientists have been actively working on the development of Hybrid energy storage devices. [5–7] Hybrid Supercapacitors (HSCs) have emerged as a promising solution that combines the advantages of both technologies. These devices integrate a battery-type electrode, which provides high energy density through faradaic redox reactions, with a capacitive counter electrode, which ensures high power density and excellent cyclic stability. Hybrids thus attempt to achieve the best of two worlds: approaching battery levels of energy density while still being a Supercapacitor in terms of high-power output as well as long cycle life.

Overall, Hybrid Supercapacitors represent an innovative advancement in energy storage technology. Their ability to bridge the gap between batteries and Supercapacitors makes them a suitable candidate for a wide range of applications, including renewable energy integration, electric vehicles, and portable electronic devices. With ongoing research and development,

Hybrid Supercapacitors hold significant potential to address the challenges of energy storage, offering a stable, efficient, and scalable solution for the future energy landscape.[9]

The electrode material forms an essential role in building effective and reliable HSCs. Negative electrodes may employ carbon-based materials such as activated carbon with the characteristic of having a high-power density, without capacity limits upon prolonged cycling. [3-10] A battery-type material that also must deliver a high level of energy density and, upon subsequent cycling, lose less capacity must comprise the positive electrode. However, oxide-based electrodes show slow reaction kinetics and poor cyclic stability, which hinder their ability to achieve a higher power density and stable lifespan. [11],[12]

Polyanion frameworks are defined as materials composed of covalently bonded $(XO_4)^{n-}$ tetrahedrons, (where X=P, S, B, C, Si, and so on), and M-O polyhedral subunits, (where M=Fe, Ni, Co, and so on). [13] Framework-type materials, which consist of polyanion frameworks, have more structural stability than oxides because the oxygen atoms are very strongly bonded to the central ion X within the tetrahedral coordination. The inductive effect of the central metal ion within the polyanionic unit also increases the ionic character of the M–O bond, thus increasing the redox potential through active participation of the $M^{n/n+1}$ redox couple.[14]-[16]

Transition metals such as nickel and cobalt-based materials are widely utilized because they are electrochemically active in alkaline solutions. Cobalt-based phosphates demonstrate pseudocapacitive behavior with high-rate performance but with relatively moderate specific capacitance. [11], [17]-[20] On the other hand, nickel-based phosphates exhibit battery-like behavior with higher specific capacitance or capacity than cobalt but at a lower rate performance. [15], [21]-[23] Thus, substituting nickel into cobalt-based materials can improve

overall electrochemical performance in general. The inclusion of Ni atoms raises active sites in electrode materials, leading to improved electrochemical performance. [24], [25]

The current work focuses on synthesis, characterization and electrochemical charge storage performance of the Nickel-substituted, Potassium Cobalt phosphate, $KCo_{1-x}Ni_xPO_4$ ($0 \leq x \leq 0.5$), where special emphasis was made on the material as $KCo_{0.5}Ni_{0.5}PO_4$, with a possible promising positive electrode material, specifically for the asymmetric Supercapacitor (ASCs) in Full Cell configuration. Electrochemical performance of $KCo_{0.5}Ni_{0.5}PO_4$ increased substantially due to the interaction of Cobalt and Nickel in synergistic manner. Specifically, it offered a charge capacity of 173 mAh/g that is equivalent to 1038 F/g capacitance, at 0.5 A/g current density within a 2M KOH aqueous electrolyte. The product maintained cyclic stability up to 5000 cycles.

In Hybrid Supercapacitor (HSC) mode, where Activated Carbon is used as the negative electrode and $KCo_{0.5}Ni_{0.5}PO_4$ as the positive electrode, the system obtained an impressive energy density of 183.7 Wh/kg and power density of 7952 W/kg in 2M aqueous KOH electrolyte. These results indicate the potential of $KCo_{0.5}Ni_{0.5}PO_4$ as a robust and high-performance positive electrode material for advanced HSCs development.

4.2 Material Synthesis and characterization

4.2.1 Synthesis of $KCo_{0.5}Ni_{0.5}PO_4$

$KCo_{0.5}Ni_{0.5}PO_4$ was synthesized using a sol-gel auto-combustion technique, which was then subjected to high temperature calcination and resulted in crystalline material. The analytical grade chemicals were employed without further purification. The used precursors have been Nickel Nitrate Hexahydrate (Merck 99.0%), Cobalt Nitrate Hexahydrate (Merck 99.0%), Potassium Carbonate (Merck 99.9%), Ammonium Phosphate (Merck 99.0%), and malic acid

(Merck 99.9%) in suitable molar concentrations for preparing $KCo_{1-x}Ni_xPO_4$. The moles of malic acid was double the sum of moles of precursors Co, Ni, and K.

For the preparation of $KCo_{0.5}Ni_{0.5}PO_4$, first of all, dissolve 0.5mM Nickel Nitrate Hexahydrate, 0.5mM Cobalt Nitrate Hexahydrate, and 1mM Potassium Carbonate in 100 ml deionized water to prepare Solution A. And, on the other hand, a solution, solution B of 1mM Ammonium Phosphate is prepared. Solution B was added slowly to Solution A, followed by the dropwise addition of 4mM Citric Acid. This formed a uniform metal-citrate complex at 100°C. It was stirred continuously for 4 hours at 80°C, and this produced a light pinkish gel.

The temperature was raised to 200°C to start the combustion process, which lasted for around 3–5 minutes and resulted in a voluminous, fluffy, brown colour material powder. The obtained material was ground and pre-treated in a muffle furnace at 400°C for 6 hours. The powder was further calcined in a furnace at 600°C for 8 hours, resulting in crystalline $KCo_{0.5}Ni_{0.5}PO_4$.
The indigo blue-coloured powder was collected and finely ground before characterization and analysis of the electrochemical performance.

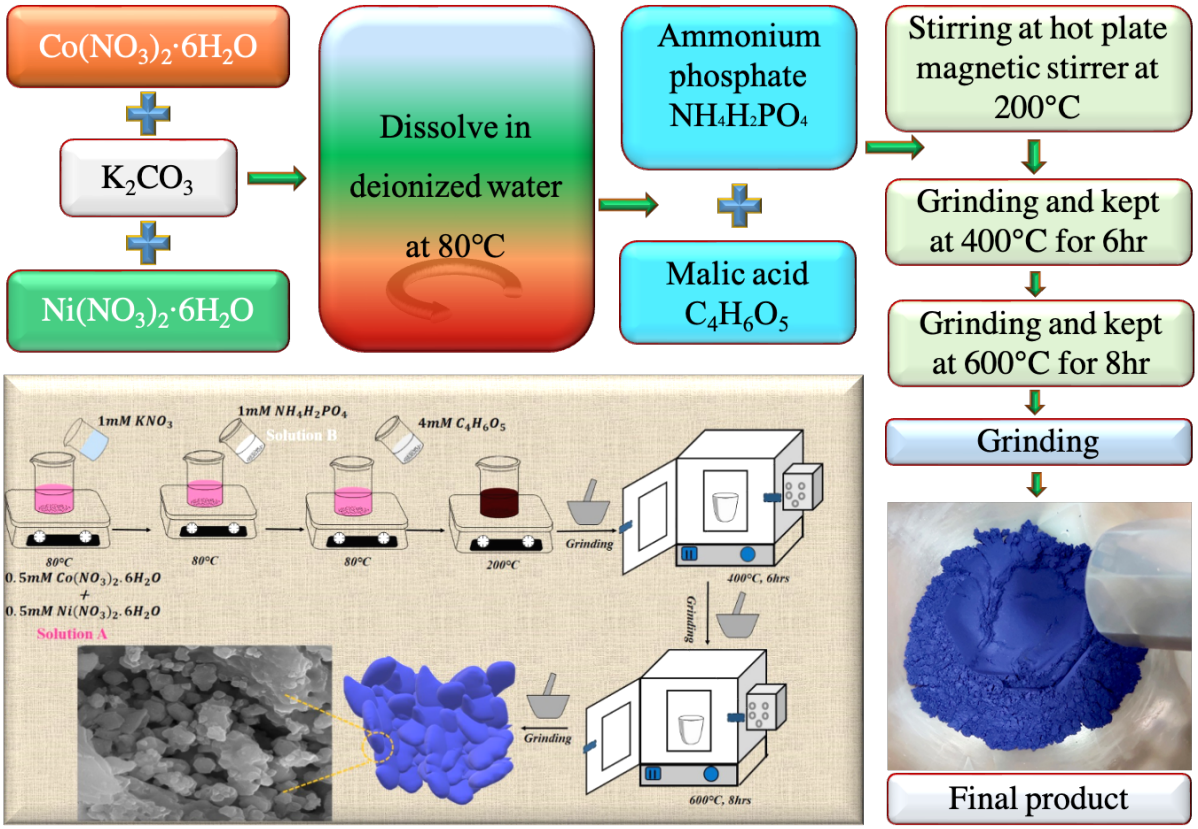

Figure 4.1: Schematic of synthesis of $KCo_{0.5}Ni_{0.5}PO_4$ sample

4.2.2 Materials characterization

The powder X-ray diffraction (XRD) analysis of all the $KCo_{1-x}Ni_xPO4$ samples was performed to examine their crystallinity and phase purity. The analysis was performed using monochromatic Cu Kα radiation (λ = 1.54056 Å) in a Rigaku Miniflex 600 benchtop X-ray diffractometer over a 2θ range of 10–60° with a step size of 0.02°. Structural identification was made using X'Pert HighScore Plus (PANalytical) software, and further crystal structure refinement was done through Rietveld refinement using FullProf Suite software.

The morphology of the synthesized $KCo_{0.5}Ni_{0.5}PO_4$ sample was examined by using an EVO Scanning Electron Microscope (MA15/18, CARL ZEISS). The Nicolet 6700 FT-IR spectrometer provided by Thermo Scientific was applied for carrying out Fourier Transform

Infrared (FT-IR) spectroscopy to determine the FT-IR spectra in range of wavenumber 400–4000 cm^{-1} for the functional groups' presence in the sample.

X-ray photoelectron spectroscopy (XPS) has been used in the determination of the elemental composition and electronic states of the sample. The acquisition of XPS spectra is made possible through a Thermo Scientific instrument equipped with a monochromatic Al Kα X-ray source.

The BET method has been used to calculate the specific surface area of the $KCo_{0.5}Ni_{0.5}PO_4$ sample. The analysis was done with the BELSORP-II analyzer from Microtrac BEL, Japan with N_2 adsorption-desorption isotherms at 77 K.

4.2.3 Electrochemical Studies

To determine the electrochemical properties of the synthesized $KCo_{0.5}Ni_{0.5}PO_4$ sample, cyclic voltammetry (CV), galvanostatic charge-discharge (GCD), and electrochemical impedance spectroscopy (EIS) measurements were carried out with a standard three-electrode system. All the measurements were carried out using Metrohm Autolab (PGSTAT204) provided with an FRA32M module for impedance analysis. Electrochemical data were analyzed with NOVA1.1 software.

4.2.4 Electrode preparation

Electrochemical tests have been carried out in a three-electrode setup which consisted of the $KCo_{1-x}Ni_xPO_4$ (x = 0, 0.1, 0.3, 0.5) as the working electrode, saturated calomel electrode (SCE)

was taken as the reference and the counter electrode was platinum plate. The electrodes were prepared using a mixture of the active material $KCo_{1-x}Ni_xPO_4$, conducting carbon (acetylene black, Alfa Aesar), and binder (PVDF, Merck) in a ratio of 70:20:10 weight %, dissolved in NMP (N-Methyl-2-pyrrolidone) solvent.

The mixture was well mixed in an agate mortar pestle to make a uniform slurry. Approximately 1 mg of the active material was applied over a 1 cm^2 section of Toray carbon paper (Alfa Aesar) and then dried at 80 °C for 12 hours to obtain the working electrode.

The material weight of the loaded electrode was determined by difference between loaded electrode and blank electrode, through the use of a Shimadzu electronic balance that had an error of 0.01 mg. The dry electrodes were then used to conduct the electrochemical tests. For measurements of full cells, i.e., Hybrid Supercapacitors, Activated Carbon was used both as a counter and as a reference electrode in 2M KOH electrolyte.

4.3 Result and discussion

4.3.1 X-ray diffraction (XRD) analysis

The XRD patterns of the powder samples $KCo_{1-x}Ni_xPO_4$ with x = 0, 0.1, 0.3, and 0.5, which are calcined at 600°C were shown in **figure 4.2**. All of the samples' XRD peaks match well with JCPDS No. 82-0762 that refers to hexagonal $KCoPO_4$.

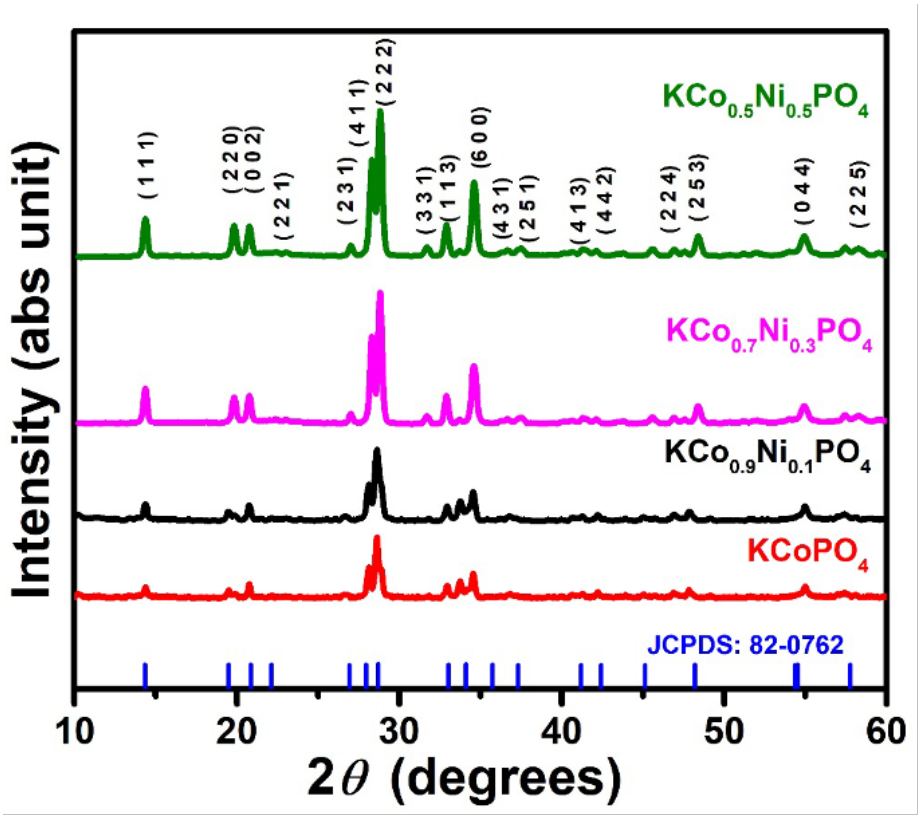

Figure 4.2: Powder XRD pattern of $KCo_{1-x}Ni_xPO_4$ (x = 0, 0.1, 02, 0.3, 0.4 and 0.5)

The Rietveld-refined powder XRD profile for calcined $KCo_{0.5}Ni_{0.5}PO_4$, as shown in **figure 4.3(a)**, confirms a good match with the

reference structure (JCPDS No. 82-0762) without the presence of any detectable impurity peaks. The lattice parameters, after refinement, are a = 18.021660 Å, b = 18.021660 Å, c = 8.604042 Å, and reliability factors are Rp = 17.5, R_{wp} = 11.4, and R_{exp} = 8.78 with χ^2 = 1.67; the formation of hexagonal crystal structure belonging to space group $P6_3$ is established.

The presence of Co-O and Ni-O polyhedral units, which are connected to each other through corner-sharing phosphate oxygen atoms, is validated from the VESTA image in **figure 4.3(b)**. The replacement of Co^{2+} ions having an ionic radius of 0.58 Å at tetrahedral sites by Ni^{2+} ions having an ionic radius of 0.55 Å shifts the peak toward a higher angle. The calculated crystallite size reduced due to this peak shift, as determined using Debye-Scherrer's equation.[26]

4.3.2 FT-IR Analysis

FTIR spectra of $KCo_{0.5}Ni_{0.5}PO_4$ powder samples in the range of wavenumber from 400 to 4000cm^{-1} are presented in **Figure 4.3(c)**. The presence of hydroxyl (-OH) group stretching vibration indicated through a broad peak at about 3400cm^{-1} suggests the presence of water in the compound.

A strong band at 1054.83 cm^{-1} is assigned to the Asymmetric stretching (ν_{as}) vibration of the P-O bond, which falls within the range of 990-1200 cm^{-1}. The symmetric stretching (ν_{ss}) vibration of P-O gives strong transmittance peaks at 944 cm^{-1} and 845.9 cm^{-1} that are due to the -PO_4 group. [27] The band at 620 cm^{-1} is assigned to O-P-O out-of-plane bending, while the band at 428 cm^{-1} is referred to -δPO_4 group. These major vibrational spectra validate the existence of the -PO_4 group in $KCo_{0.5}Ni_{0.5}PO_4$.

Besides, the Asymmetric stretching modes of CoO_6 octahedra are found at 587 cm^{-1},[28] whereas the peak near 549 cm^{-1} is attributed to the Asymmetric stretching of Ni-O bonds in NiO_6 octahedra. [29] The absorption peak at 479 cm^{-1} is due to both Ni-O and Co-O bonding in the synthesized $KCo_{0.5}Ni_{0.5}PO_4$ sample. [30]

4.3.3 Brunauer-Emmett-Teller (BET) Analysis

To evaluate the surface area and pore volume of the sample, the N_2 adsorption-desorption isotherm measured at 77K is presented in **figure 4.3(d)**. The isotherm represents type III with an H3 hysteresis loop, indicating the presence of mesoporous structures that are connected through macropores. [31], [32] A slight hysteresis appearing at high relative pressure range in the N_2 adsorption-desorption isotherm also testifies to capillary condensation phenomenon, that affirming its mesoporous character. [33] This pre-treated sample has a specific surface area of around about 25.875 m^2/g along with major pore size range from 3 to 10 nm and few macropore

at the size of around 220 nm according to BJH (Brunauer, Joyner, and Halenda) plot of inset of **figure 4.3(d)**. As mesoporous moieties of this material make it prone to exhibit some better electrochemical activities by virtue of its higher porous nature. The average pore diameter of the $KCo_{0.5}Ni_{0.5}PO_4$ sample was calculated to be ~20.79 nm.

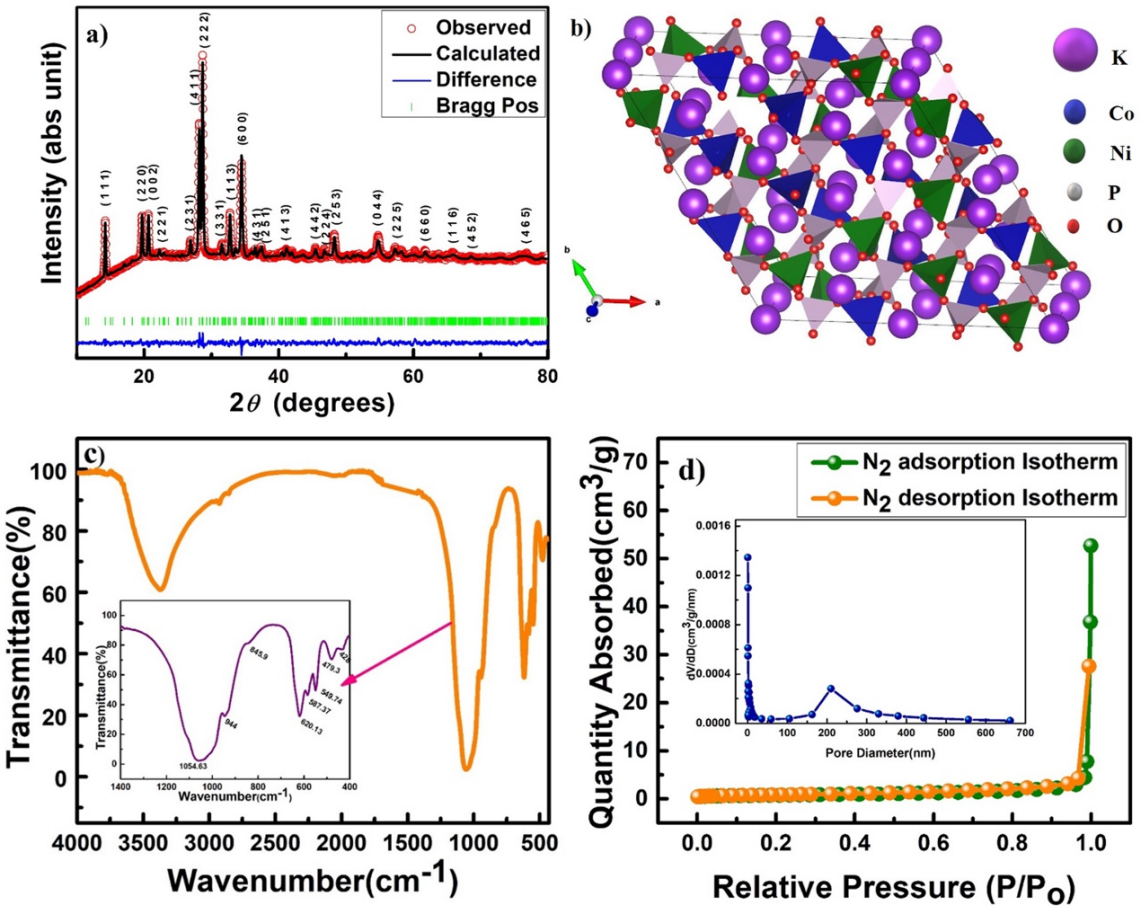

Figure 4.3: (a) XRD Rietveld refinement pattern of $KCo_{0.5}Ni_{0.5}PO_4$ powder sample (b) VESTA image of $KCo_{0.5}Ni_{0.5}PO_4$ (blue, green, grey are tetrahedra of Co-O, Ni-O and P-O, respectively)(c) FTIR spectrum of $KCo_{0.5}Ni_{0.5}PO_4$ (d) N_2 adsorption/desorption isotherm of $KCo_{0.5}Ni_{0.5}PO_4$ sample

4.3.4 X-ray photoelectron spectroscopy (XPS) Analysis

Chemical composition and valence states of elements present in the sample $KCo_{0.5}Ni_{0.5}PO_4$ are analyzed through XPS (X-ray photoelectron spectroscopy). Broad survey spectrum in **figure**

4.4(a) supports the existence of K, Co, Ni, P, and O in the sample. From **figure 4.4(b)**, the two binding energies of K $2p_{3/2}$ and K $2p_{1/2}$ were observed at the binding energy value of 292.2 eV and 295.1 eV, which confirm the presence of K^+ ions in the compound.

The Co(2p) spectrum in **figure 4.4(c)** splits into peaks with separations associated with the $2p_{3/2}$ state of Co^{2+} at 780.63 eV and the $2p2p_{1/2}$ state at 796.41 eV. In addition to the peaks associated with Co^{2+} ions, satellite peaks appear at 784.17 eV and 801.96 eV. In the Ni(2p) core level spectrum, shown in **figure 4.4(d)**, the Ni $2p_{3/2}$ and Ni $2p_{1/2}$ states are found to correspond to binding energies of 855.6 eV and 873.4 eV, respectively. Each state is accompanied by satellite peaks at 860.9 eV and 879 eV. All the aforesaid values ascertain that the sample contains Ni as Ni^{2+}.

Figure 4.4(e) displays the O(1s) spectrum state of the $KCo_{0.5}Ni_{0.5}PO_4$ with two evident peaks at 530.8 eV corresponding to metal-oxygen bonds Ni-O and Co-O while the second peak is situated at 532.2 eV related to P-O bonds.[34] Finally, **Figure 4.4(f)** P(2p) is split into the P $2p_{3/2}$ and P $2p_{1/2}$ states with their binding energies at 132.41 eV and 133.47 eV, which confirms the presence of P^{5+} ions within the PO_4 unit.

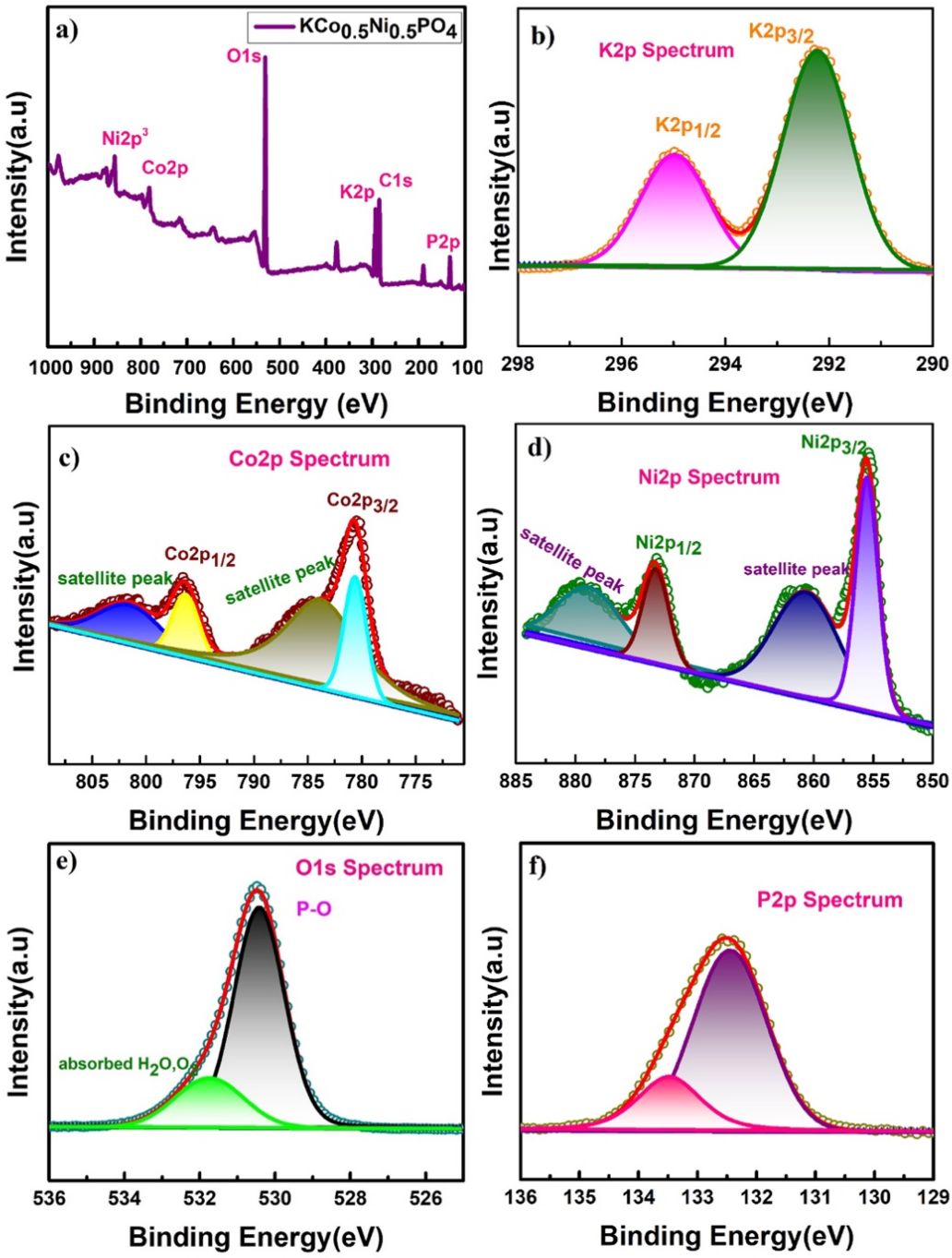

Figure 4.4: XPS of $KCo_{0.5}Ni_{0.5}PO_4$ of powder sample; (a) full survey, (b) K (1s), (c) Co(2p), (d) Ni(2p), (e) O (1s) and (f) P (2p)

4.3.5 SEM Analysis

The morphological characteristics of the synthesized $KCo_{1-x}Ni_xPO_4$ (x = 0, 0.1, 0.3, and 0.5) samples were characterized by using electron microscopy techniques. **Figure 4.5(a)** displays the FE-SEM image of the $KCo_{0.5}Ni_{0.5}PO_4$ sample with the particle morphology and surface structure composed of flake-like arrangements with an average particle size of 437 nm.

Elemental analysis by Energy Dispersive X-ray Analysis shown in **figure 4.5(b)**, presents the peaks for all of the constituent elements, that are K, Co, Ni, P, and O in $KCo_{0.5}Ni_{0.5}PO_4$. Moreover, FE-SEM mapping, as shown in the **figures 4.5(c-g)**, confirms the uniform distribution of K, Co, Ni, P, and O throughout the material of the electrode, pointing toward their presence in a pure form within the synthesized product.

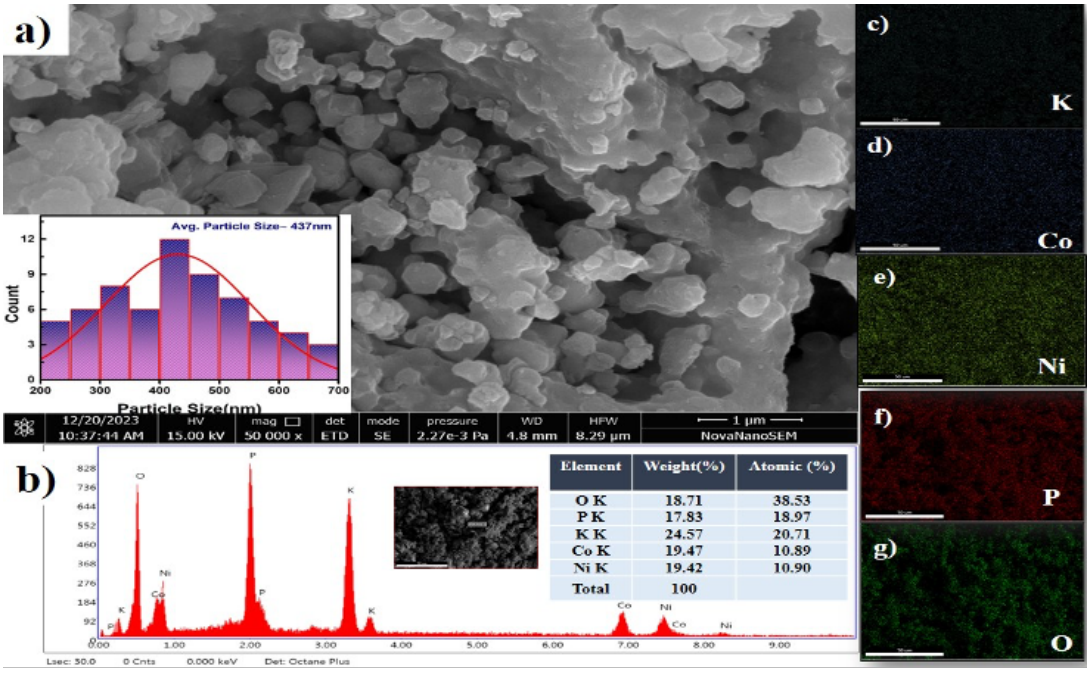

Figure 4.5: (a) Particle distribution of $KCo_{0.5}Ni_{0.5}PO_4$ in SEM image, (b) elemental analysis of $KCo_{0.5}Ni_{0.5}PO_4$ by EDX. (c)-(g) Colour mapping of the element present in $KCo_{0.5}Ni_{0.5}PO_4$.

4.3.6 Transmission electron microscopy (TEM) Analysis

In **figure 4.6**, the high-resolution transmission electron microscopy (HR-TEM) images of the $KCo_{0.5}Ni_{0.5}PO_4$ sample are provided. **Figure 4.6(a)** shows the lattice fringes of the sample, whereas the fast Fourier transformation and the inverse FFT images of the sample are shown in **figures 4.6(a)(i-ii)**. As shown in **figure 4.6(b)**, the measured lattice fringe thickness is about 0.252 nm, corresponding to the (600) plane of the synthesized $KCo_{0.5}Ni_{0.5}PO_4$ sample.

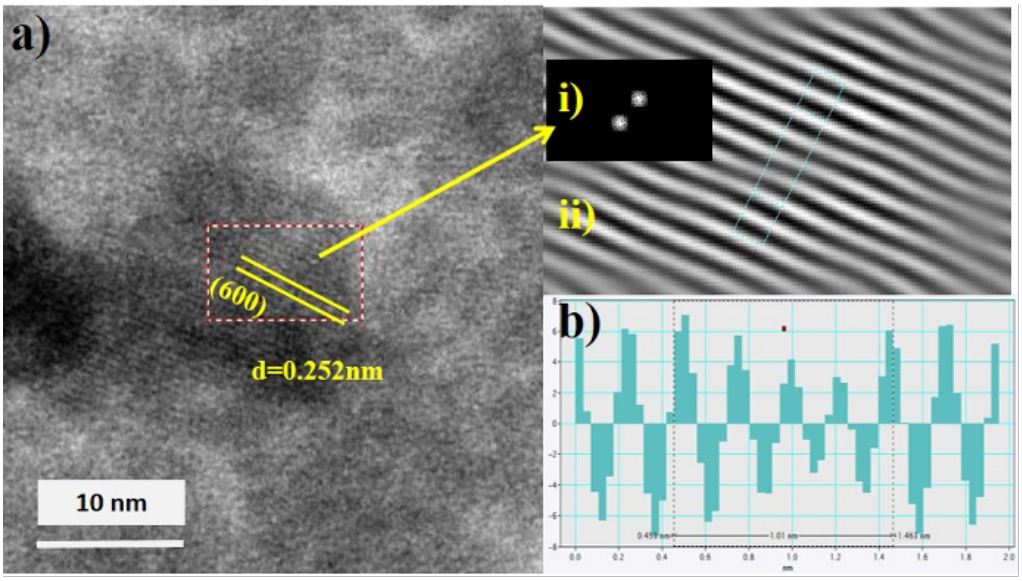

Figure 4.6: (a) visible lattice fringes containing 600 planes in HRTEM image, **(i-ii):** FFT and inverse FFT images of the selected region of the (600) plane. (b) shows d spacing of fringes that matches with the (600) plane of the $KCo_{0.5}Ni_{0.5}PO_4$ lattice.

4.4 Electrochemical Studies

4.4.1. Half-cell (three-electrode electrochemical cell) measurements

Figure 4.7 presents the Cyclicvoltagram (CV) plots for all $KCo_{1-x}Ni_xPO_4$ (x = 0, 0.1, 0.3, and 0.5) samples within a 2M KOH electrolyte, as recorded at a scan rate of 5 mV/s within the voltage range of 0–0.6 V. In the case of $KCoPO_4$, the near-rectangular shape is observed in the CV curve, which suggests capacitive charge storage behavior. On further Ni doping, redox peaks start to appear in the CV plots. With an increase in Ni content, the intensity of these redox peaks rises along with a larger area under the CV curve, which implies an enhancement in the charge storage capacity of the Ni-doped $KCoPO_4$ samples. The electrochemical characteristics of the prepared samples were analyzed by determining the charge storage capacity from Equation (4.1).

$$\mathrm{Csp} = \frac{\int \mathrm{i}\,(\mathrm{V})\mathrm{dV}}{2\mathrm{mV}\vartheta} \tag{4.1}$$

The specific charge storage capacity in mAh/g can be calculated using eq.(4.2).

$$C\left(\frac{mAh}{g}\right) = Csp * \Delta V = \frac{\int i\,(V)dV}{2m\vartheta * 3.6} \tag{4.2}$$

Where ‘m’ is the active mass of the electrode (g), ‘V’ is the operating voltage window (V), and ‘ϑ’ is the scan rate (mV/s).

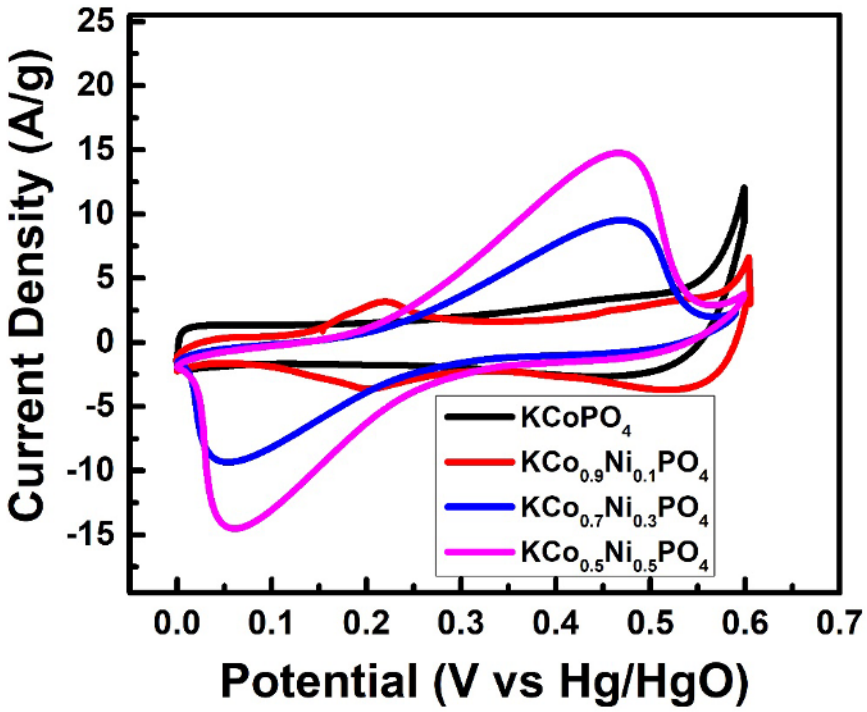

Figure 4.7: Comparative CV of $KCo_{1-x}Ni_xPO_4$ (x = 0, 0.1, 0.3 and 0.5) in 2M KOH electrolyte solution and 5mV/s scan rate.

The charge storage capacities of $KCo_{1-x}Ni_xPO_4$ (x = 0, 0.1, 0.3, and 0.5) samples were measured at a scan rate of 5 mV/s in 2M KOH electrolyte as 575 F/g, 623 F/g, 735 F/g, and 845 F/g, respectively. Among the samples, the $KCo_{0.5}Ni_{0.5}PO_4$ sample had the highest charge storage performance and had a very sharp redox peak. Therefore, to further evaluate the electrochemical performance of this material, cyclic voltammetry (CV), galvanostatic charge-discharge (GCD), and electrochemical impedance spectroscopy (EIS) were done in three-electrode configuration and 2M KOH as the electrolyte.

Figure 4.8(a) shows the CV curves of $KCo_{0.5}Ni_{0.5}PO_4$ at various scan rates, showing separated redox peaks in the potential window of 0 V to 0.6 V. The CV curve emphasizes the redox mediated intercalation storage along with surface redox (electrosorption) behavior. Thus, it is

confirmed that charge storage happens through an intercalative type of redox-mediated process. The redox peaks are due to the reversible transformation between Co^{2+}/Co^{3+} and Ni^{2+}/Ni^{3+} by the electrosorption of OH^- ions according to equation (4.3).

redox-mediated diffusion controlled intercalation reaction

$$KCo_{0.5}(II)Ni_{0.5}(II)PO_4 + OH^-_{sol} \leftrightarrow KCo_{0.5}(III)Ni_{0.5}(III)(OH^-)PO_4 + e^- \quad (4.3)$$

EDLC-type surface capacitance reaction

$$KCo_{0.5}(II)Ni_{0.5}(II)PO_4 + xKOH \leftrightarrow K^+_x \,|\, KCo_{0.5}(II)\, Ni_{0.5}(II)PO_4 \,|\, xOH^- \quad (4.4)$$

Total charge storage capacity reaction

$$KCo_{0.5}(II)Ni_{0.5}(II)PO_4 + OH^- \leftrightarrow K^+_x \,|\, KCo_{0.5}(II)Ni_{0.5}(II)PO_4 \,|\, OH^-_{(1+x)} + xe^- \quad (4.5)$$

The charge storage capacity of $KCo_{0.5}Ni_{0.5}PO_4$ was measured by using equations (4.1) and (4.2); that gave about 142.3 mAh/g, which corresponds to a capacitance of 854 F/g at a scan rate of 0.5 mV/s. A linear increase of both the anodic and cathodic peaks with increasing scan rates was observed, and charge storage in the material appears to be dominated by diffusion-controlled, intercalative redox processes. **Figure 4.8(b)** plots the dependency of the anodic and cathodic peak currents upon the square root of scan rate, showing a clear linear relationship and further reiterating that the reaction mechanism is a semi-infinite diffusion-controlled redox reaction mechanism for the electrode $KCo_{0.5}Ni_{0.5}PO_4$. Electrode kinetics were also assessed by considering the ion diffusion coefficient evaluated using the Randles-Sevick equation as reported previously in: [35], [36]

$$i_p = 2.686 \times 10^5 \times n^{3/2} A D^{1/2} C_o v^{1/2} \quad (4.6)$$

Where i_p is peak current density (A), n is the number of electrons that participated in the redox reaction (usually 1), A is the area of the electrode in cm^2, D is diffusion coefficient in cm^2/s, C_o is OH^- ion concentration in mol/cm^3 and ν is scan rate in V/s. By using equation (4.6), the

diffusion coefficient (D) of OH^- in the $KCo_{0.5}Ni_{0.5}PO_4$ electrode was found $1.47\times10^{-8}cm^2/s$ for the oxidation reaction and $1.38\times10^{-8}\ cm^2/s$ for the reduction reaction.

To further understand the electrochemical kinetics of charge storage behaviour of electrodes in aqueous electrolytes, or to understand the qualitative nature of the charge storage mechanism of $KCo_{0.5}Ni_{0.5}PO_4$ electrode by investigating the correlative contribution of the battery type or the capacitive type nature using the power-law equation given below in eq.(4.7): [35]

$$i = av^b \qquad (4.7)$$

Where, a and b are adjustable parameters, i is the current (A), and ν is the scan rate (V/s). The values of b range from 0.5 to 1 b = 0.5 stands for the intercalative semi-infinite diffusion control redox process or battery-type charge storage behaviour while b = 1 stands for the capacitive control reaction.

For the determination of b value **figure 4.8(c)** shows the log (peak current (i_p) vs log (v) plots and from the slope that plot, b values are extracted. From that instance, for scan rates of 0.5mv/s to 5mv/s, the b-value of current observed for anodic peak is found close to 0.623 and for the cathodic peak it was found close to 0.651, that value indicating the rate kinetics are controlled by semi-infinite diffusion-controlled intercalating process rather than capacitive.

The scan rate dependence on current density plot can be utilized for quantitative assessment of contributions from capacitive and ion intercalation processes at lower scan rates, as in **figure 4.8(d)**. Dunn's method applies equation (4.8) for the separate isolation of the capacitive and diffusion-controlled charge storage in electrodes into two components. [15], [30], [37]

$$i(\upsilon) = k_1 v + k_2 v^{\frac{1}{2}} \qquad (4.8)$$

Equation (4.8) was simplified into equation (4.9) to separate the total charge stored into the peculiar contributions.

$$i(\upsilon)/v^{(1/2)} = k_1/v^{(1/2)} + k_2 \qquad (4.9)$$

From eq. (4.9), k_1 and k_2 account for the current contribution from the surface capacitance and the diffusion-controlled intercalation charge storage, respectively. In consequence, the current response i(V) is extracted from CVs obtained over a range of scan rates, and the slope of a linear fit provides a constant value of the constant k_1, as well as a y-intercept corresponding to the value of the constant k_2, when plotting $i(V)/v^{1/2}$ vs $v^{1/2}$, as shown in **figure 4.8(d)**. As illustrated by **figure 4.8(e)**, after calculating k_1 and k_2 values, surface-controlled charge storage contribution approached approximately 37.7% and the contribution for diffusion-controlled interaction process approached almost 62.3 % at 0.31 V peak potential with the scan rate of 0.5 mV/s. Contribution of diffusion controlled intercalative and surface-controlled charge storage at various scan rates is depicted by **figure 4.8(f)**.

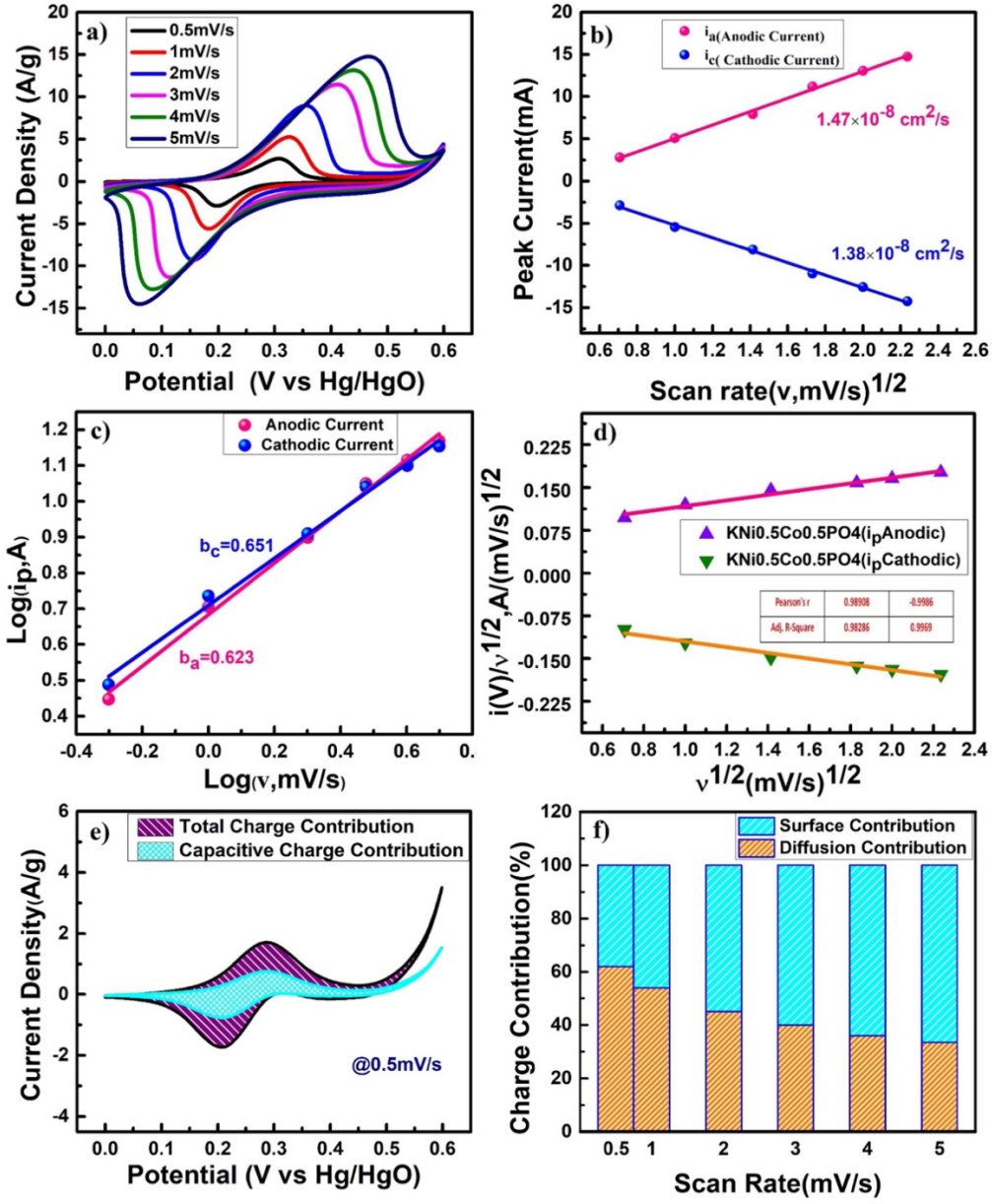

Figure 4.8: (a) cyclic voltammetry of $KCo_{0.5}Ni_{0.5}PO_4$ electrode in 2 M KOH electrolyte, (b) peak current density vs square root of the scan rates plot, (c) plot of log (peak current) vs log (scan rate) presenting b Values, (d) capacitive and diffusion control process contribution in the current density at the scan rate of 0.5 mV/s, (e) presenting surface capacitance and diffusion-controlled interaction process contribution at a scan rate 0.5 mV/s on the charging peak potential equal to 0.31V and (f) capacitive and diffusion control process contribution at different scan rates.

According to Trassati the amount of charge stored in the outer and inner surfaces was calculated using the Trasatti plot. As suggested by Trassati, the total charge storage capacitance of a material is the aggregate of the inner and outer surface contribution to the capacitance of the electrode and is represented by eq. (4.10): [11],[15][35]

$$C_{total} = C_{in} + C_{out} \text{ (F /g)} \qquad (4.10)$$

The charge storage capacitance of the inner and outer surfaces of the electrode varies as the square root of the scan rate. The y-intercept of the linear fit of C^{-1} versus $\nu^{1/2}$ for various scan rates is seen in **figure 4.9(a)**, and it is determined by the total charge stored or the total capacitance of the electrode. This again, as with the curve in **figure 4.9(b)**, the y-intercept of the linear C vs. $\nu^{1/2}$ curve indicates that the outer surface charge storage contribution or the capacitance that arises from the outer part of the electrode (C_{out}). Applying this Trasatti plot analysis, the total charge held in the electrode was obtained as about 142.3 mAh/g (specific capacitance: 854 F/g) at 0.5 mV/s. The inner surface contribution to the total capacitance was 91 mAh/g (546 F/g, 64% of the total capacity), and the outer surface contribution (C_{out}) was 51.3 mAh/g (308 F/g, 36% of the total capacity). Conclusion: Thus, it can be concluded that charge storage is primarily due to a semi-infinite diffusion-controlled mechanism in the electrode.[38]

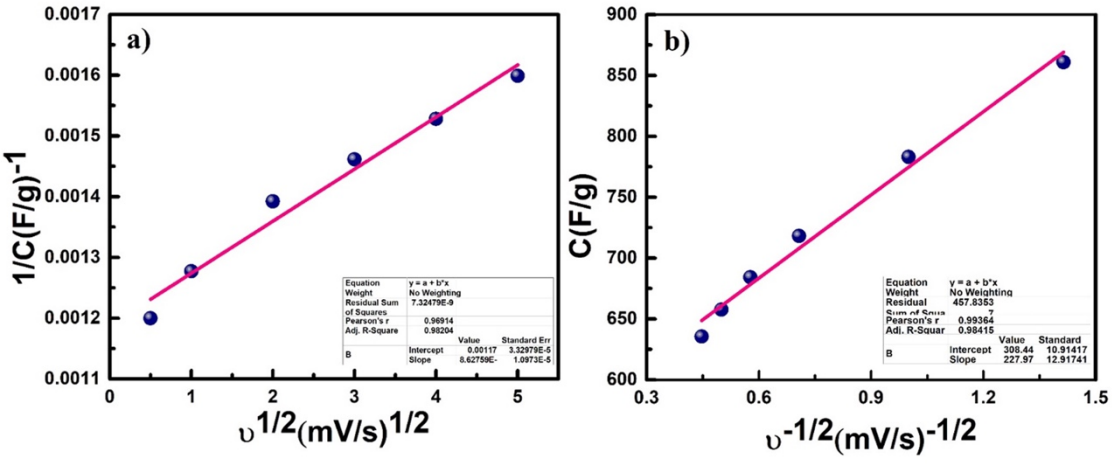

Figure 4.9: (a) C^{-1}*vs.* $v^{1/2}$ (b) *C vs.* $v^{-1/2}$ derived from Trasatti's method.

GCD analysis was conducted within the voltage range of 0–0.6 V at both constant and varying current densities to further assess the charge storage performance. By examining GCD curves at different discharge currents, the electrode's charge storage capacity (total capacitance) can be determined using equation (4.11). [39], [40]

$$\mathrm{Csp} = \frac{\mathrm{I}\Delta\mathrm{t}}{\mathrm{m}\Delta\mathrm{V}} \quad (4.11)$$

The specific capacity of the electrode in mAh/g is calculated by modifying equation (4.11) as represented below.

$$C\left(\frac{mAh}{g}\right) = Csp * \Delta V = \frac{I\Delta t}{m*3.6} \quad (4.12)$$

Where I is the discharge current density (A), Δt is the discharge time (s), m is the active mass of the electrode (g) and ΔV is the potential window of the discharge (V).

The Galvanostatic charge/discharge capacity and capacitances of $KCo_{0.5}Ni_{0.5}PO_4$ were shown in **figure 4.10(a)**, whose values are measured at 173 mAh/g (1038 F/g), 144.3 mAh/g (865.8 F/g), 115.5 mAh/g (693 F/g), 85.8 mAh/g (515 F/g), 61.2 mAh/g (367.6 F/g), and 37.4 mAh/g (224.4 F/g) for current rates of 0.5, 1, 2, 3, 4, and 5 A/g, respectively. The GCD curves of the $KCo_{0.5}Ni_{0.5}PO_4$ electrodes show stable and symmetric charge/discharge behavior, which indicates a pseudocapacitive nature due to redox-mediated intercalating storage. The GCD experiments reveal a higher capacity than cyclic voltammetry, indicating more diffusion-controlled bulk charge storage, confirming the redox-mediated battery-type intercalating charge storage in the material. **Figure 4.10(b)** shows the specific capacity of $KCo_{0.5}Ni_{0.5}PO_4$ at different current densities (0.5 to 5 A/g) over multiple cycles. The capacity decreases as the current density increases. Importantly, when the current density is restored to 1 A/g after testing at higher rates, the specific capacity of $KCo_{0.5}Ni_{0.5}PO_4$ is stable. **Figure 4.10(c)** shows the excellent cycle stability of $KCo_{0.5}Ni_{0.5}PO_4$ at 5 A/g for 5000 cycles with a capacity retention of 88.93% after 5000 cycles. In this regard, the same figure also exhibits the coulombic efficiency ($\eta = {}^{t_d}/_{t_c}$)of the electrode around 5000 charge/discharge cycles ~97.2%, which illustrates excellent reversibility and stability during such performance. In addition to these, the long-term electrochemical performances of $KCo_{0.5}Ni_{0.5}PO_4$ are evaluated using Electrochemical

Impedance Spectroscopy (EIS), shown in the Nyquist plot in **figure 4.10(d)** before and after the cycling stability test; here, slight changes of the solution resistance (R_s) from 1.23 to 1.52 are noticed. It exhibited increased charge transfer resistance R_{ct} from 0.55 to 0.81, which can be said due to the electrolyte accumulation around the KOH/ $KCo_{0.5}Ni_{0.5}PO_4$ interface.[37] Even total resistance (a summation of R_s and R_{ct}), that means the ESR, slightly increased, going from 1.78 Ω to 2.35 Ω, demonstrating the $KCo_{0.5}Ni_{0.5}PO_4$ material's superior performance.

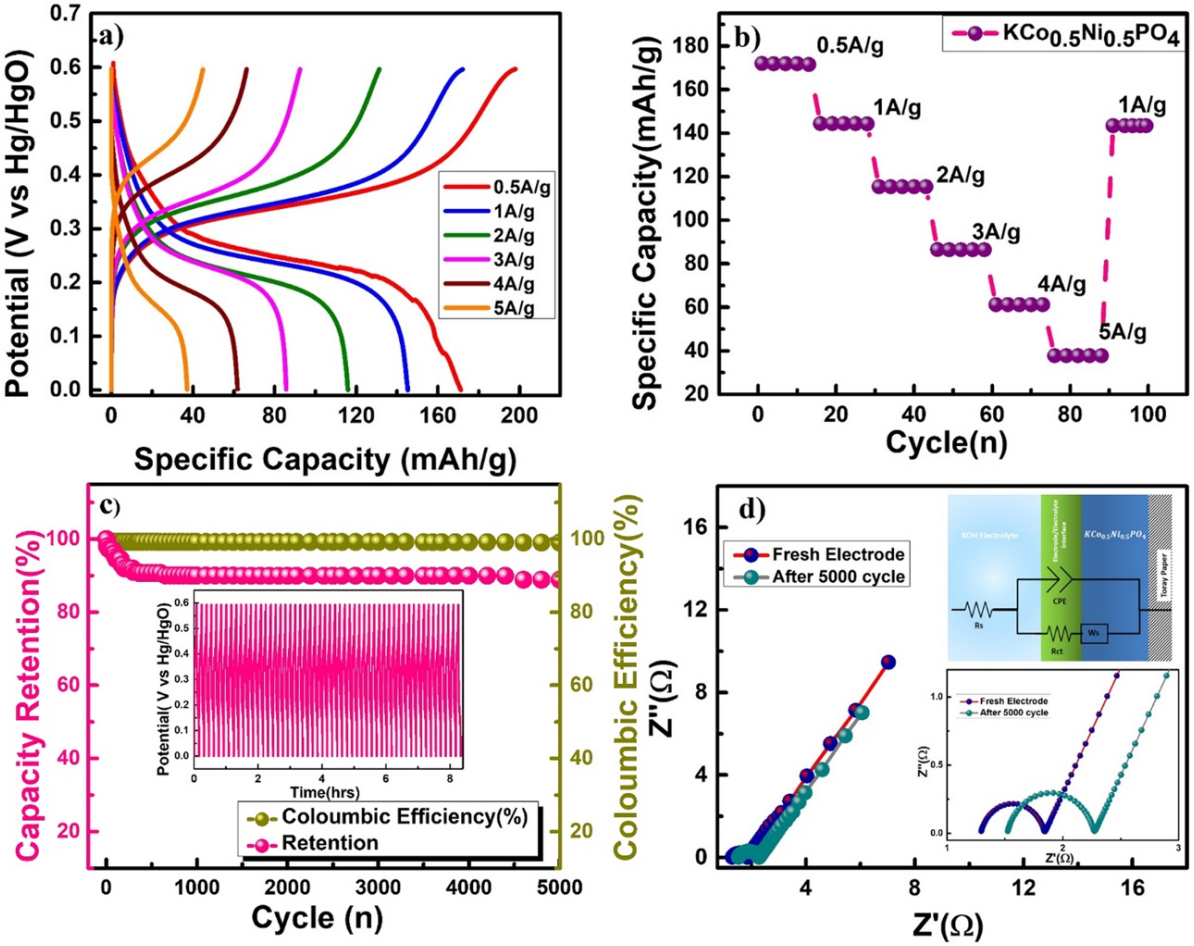

Figure 4.10: (a) Charge/discharge plot (V vs time) of the $KCo_{0.5}Ni_{0.5}PO_4$ electrode at various constant current rates (0.5, 1, 2, 3, 4 and 5A/g), (b) capacity/capacitance performance of the $KCo_{0.5}Ni_{0.5}PO_4$ in 2 M KOH electrolyte at different current densities, (c) Capacity retention and Coulombic efficiency plot and (d) Nyquist plot before and after cycle at 10 mV applied voltage in the frequency range of 1 MHz to 0.1 Hz.

4.4.2 Full cell measurements in Hybrid Supercapacitor (HSCs) Mode

A Hybrid Supercapacitor (HSC) was prepared based on $KCo_{0.5}Ni_{0.5}PO_4$ as the positive electrode along with Activated Carbon (AC) as the negative electrode in the 2M KOH electrolyte to demonstrate its versatility. The charge storage ability of both the electrodes of the full-cell test will be optimized through the help of the following equation:

$$\frac{1}{C_{total}} = \frac{1}{C_{positive}} + \frac{1}{C_{negative}} \quad (4.13)$$

In order to maintain the charge storage capacitance of each electrode in balance within the cell, the mass ratio (m+/m-) of the two electrodes was determined using the following equation (4.14):

$$\frac{m^-}{m^+} = \frac{C_+ \times \Delta E_+}{C_- \times \Delta E_-} \quad (4.14)$$

Where $m^+, m^-, C_+, C_-, \Delta E_+, \Delta E_-$ are both electrodes' active mass, specific capacitance, and potential window.

Figure 4.11(a) shows independent CV profiles of the activated carbon (AC) negative electrode and the $KCo_{0.5}Ni_{0.5}PO_4$ positive electrode. The active mass ratio ($\frac{m^-}{m^+}$) of the electrodes was established to be 3.1:1. **Figure 4.11(b)** shows CV curves of the AC// $KCo_{0.5}Ni_{0.5}PO_4$ full cell under two-electrode Hybrid Supercapacitor (HSC) operation mode at a potential range of 1.6 V, scanned from 1 mV/s to 100 mV/s.

Figure 4.11(c) displays the full cell's quantitative charge storage capability using galvanostatic charge-discharge measurements plot. The capacity and capacitance values were calculated using Equation (4.10) and the charge storage capacity of the Hybrid Supercapacitor was measured as 228.3 mAh/g (514 F/g), 174.8 mAh/g (394 F/g), 112.5 mAh/g (254 F/g), 77.2 mAh/g (173.7 F/g), and 45.57 mAh/g (102.5 F/g) at respective current densities of 0.5 A/g, 1 A/g, 2.5 A/g, 5 A/g, and 10 A/g.

Figure 4.11(d) shows the electrochemical impedance spectroscopy (EIS) spectra results in the form of Nyquist plots recorded within a frequency range of 1 MHz to 0.1 Hz with an applied potential of 10 mV/s both before and after cycling. From the Nyquist plot, the resistance of the solution (R_s) increased from 1.44 Ω, as measured before cycling, to 2.12 Ω, as measured after cycling, while the charge transfer resistance (R_{ct}) increased from 5.03 Ω to 7.86 Ω after the life cycle test. The variations of resistance in the EIS spectra show that the superior capacitive performance is due to improved charge transfer within the AC// $KCo_{0.5}Ni_{0.5}PO_4$ full cell.

The Hybrid Supercapacitor (HSCs) based AC// $KCo_{0.5}Ni_{0.5}PO_4$ full cell had an excellent Coulombic efficiency of around 96% and exhibited remarkable stability, maintaining 87.2% of its capacitance after 5000 cycles which is shown in **figure 4.4.5(e)**.

The specific energy density (E) and specific power density (P) of the Hybrid Supercapacitor were computed using the following equations.

$$E(Wh/kg) = \frac{1}{2}\frac{C_{HSCs}}{3.6}V^2 \qquad (4.15)$$

$$P(W/kg) = \frac{E*3600}{t_{dis}} \qquad (4.16)$$

Where C_{HSCs} is specific capacitance, V is Potential window and t_{dis} is discharge time.

Figure 4.11(f) is a Ragone plot, which is energy density against power capacity plot at constant current densities of various values. The performance of the full cell based on AC// $KCo_{0.5}Ni_{0.5}PO_4$ was excellent, with a peak value of 183.7 Wh/kg at a current rate of 0.5 A/g (or a power capacity close to 414 W/kg). The full cell at a current density of 10 A/g was able to attain a maximum power density of 7952 W/kg, along with an energy density of 36 Wh/kg.

Such remarkable full-cell performances in the two-electrode Hybrid Supercapacitor configuration for HSC development highlight the suitability of the $KCo_{0.5}Ni_{0.5}PO_4$ electrode for creating superior Hybrid Supercapacitors.

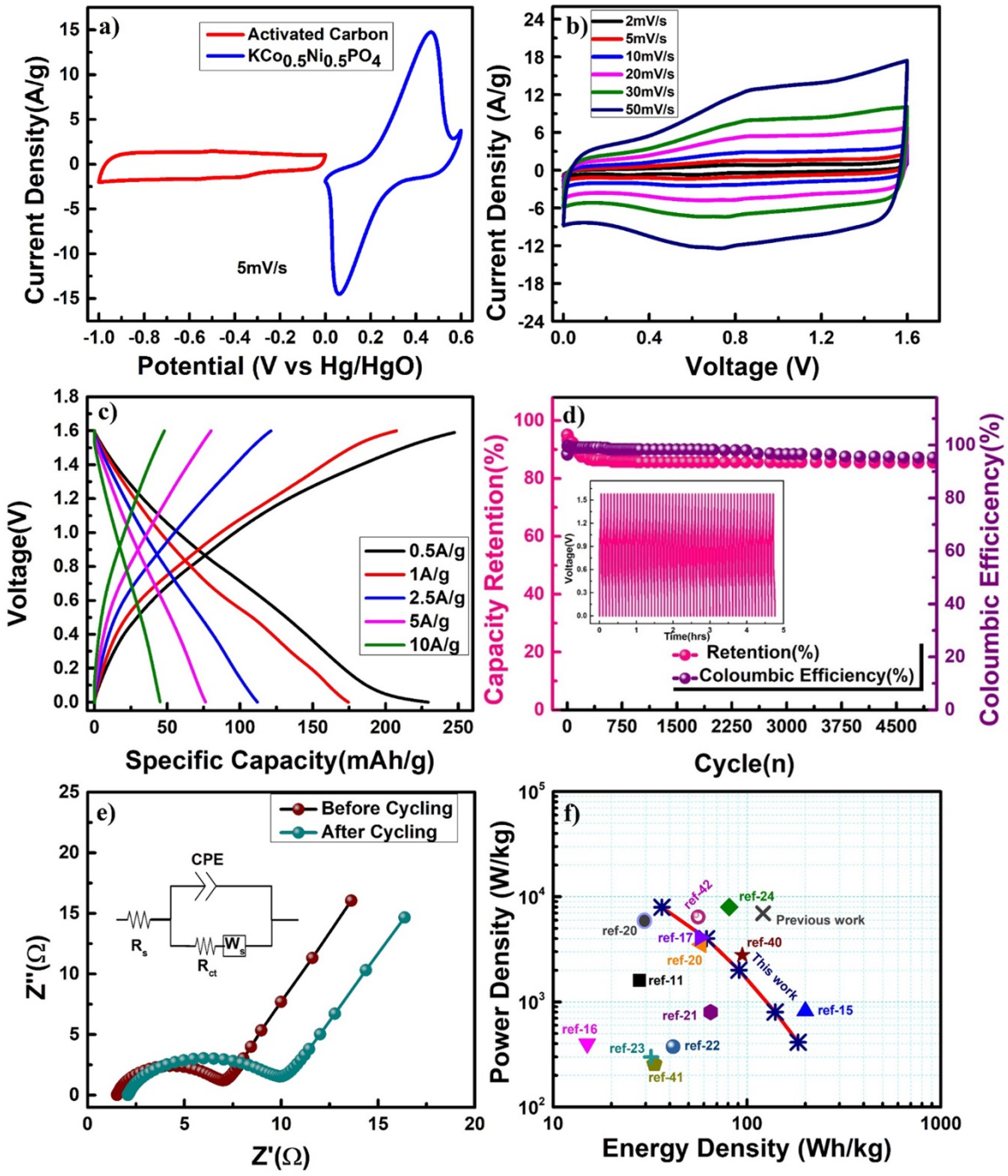

Figure 4.11: (a) CV curves AC and $KCo_{0.5}Ni_{0.5}PO_4$ electrode at 5 mV/s in a three-electrode system, (b) CV curves of AC//$KCo_{0.5}Ni_{0.5}PO_4$ as HSCs in 2MKOH at different scan rates, (c) Specific capacity of AC// $KCo_{0.5}Ni_{0.5}PO_4$ as HSCs in 2MKOH at different current density, (d) capacitive retention and coulombic efficiency of the HSCs device, (e) Nyquist at initial cycle and after 5000 cycles of the full cell in HSCs mode (f) Ragone plot of AC// $KCo_{0.5}Ni_{0.5}PO_4$ as HSCs with another literature report.

Furthermore, in HSC mode, a performance comparison of several phosphate-based transition metal phosphate electrodes is presented in **Table 4.1.** [11], [15]–[18], [20]–[24], [40]–[42] Such a comparison again underlines the higher performance of the full cell in HSC mode of

$KCo_{0.5}Ni_{0.5}PO_4$ electrode. Therefore, $KCo_{0.5}Ni_{0.5}PO_4$ electrode, displaying battery-type intercalation behavior, stands as an attractive material for the production of high-performance Hybrid Supercapacitors.

Table 4.1 Comparative Study of Electrochemical Performances of Cobalt and Nickel based Phosphate Electrode Materials in Full Cell.

Electrode material (Negative Electrode//Positive Electrode)	**Electrolyte**	**Specific Capacitance**	**Energy density /Power Density**	**Ref.**
AC//γ-$KCoPO_4$	1M KOH	100 C/g at 0.6 mA/cm^2	ED=28 Wh/kg at PD=1600W/kg	[11]
AC//$KNiPO_4$	2MKOH	168.5 mAh/g (Capacitance: 935 F/g) at 1 A/g	ED=200 Wh/kg PD=819 W/kg	[15]
AC// $NaMn_{1/3}Ni_{1/3}Co_{1/3}PO_4$	2M NaOH	45 F/g at 0.5A/g	ED=15 Wh/kg PD=400 W/kg	[16]
AC// $Co_2P_2O_7$/MWCNT	1M KOH	114 mAh/g at 2.9A/g	ED=57.3 Wh/kg at PD=4100 W/kg	[17]
AC// $Co_3(PO_4)_2$	1M NaOH	111.2 F/g at 5mA/cm^2	ED=29.20 Wh/kg at PD= 4687 W/kg	[18]
AC// $Co_3(PO_4)_2 \cdot 8H_2O$	1M KOH	163 F/g at 2mA/cm^2	ED=58.12 Wh/kg at PW=3520 W/kg	[20]
HPGC//$Ni_2P_2O_7$	1M NaOH	183F/g at 1A/g	ED= 65 Wh/kg at PD=800W/kg	[21]
AC//$NH_4NiPO_4 \cdot H_2O$	3M KOH	1513 F/g at 5 A/g	ED= 41.6 Wh/ kg at PD= 375 W/kg	[22]
AC// $NaNiPO_4$	2M NaOH	90 F/g at 0.3A/g	ED= 32 Wh/kg at PD= 300 W/kg	[23]
AC// $KCo_{0.33}Ni_{0.67}PO_4 \cdot H_2O$	1M KOH	227F/g at 1.5A/g	ED=80.64 Wh/kg at PW=8000 W/kg	[24]
AC// $CoNiP_2O_7$/NF@PPy	2M KOH	390mAh/g at 2A/g	ED= 94.6Wh/kg at PD=2791W/kg	[41]

AC// $Ni_2P_2O_7/Co_2P_2O_7$	2M KOH	2074F/g at 5A/g	ED= 33.3 Wh/kg at PD= 257 W/kg	[42]
AC//$Co_{0.125}Cu_{0.375}Mn_{0.5}(PO_4)_2$	1M KOH	158.5F/g @1A/g	ED=56Wh/kg at PD=6420W/kg	[43]
AC//KCoPO4	2M KOH	387F/g at 1A/g	ED=121 Wh/kg at PD= 6945 W/kg	Previous work
AC//$KCo_{0.5}Ni_{0.5}PO_4$	2MKOH	173mAh/g @0.5A/g	ED=183.5Wh/kg at PD=7952W/kg	This work

4.5 Conclusions

Synthesis done of powder $KCo_{1-x}Ni_xPO_4$ with x = 0, 0.1, 0.3, and 0.5 through the sol-gel auto-combustion method followed by high temperature calcination at 600°C in air, as a two-step process has proven the ability for successful preparation of a strong phosphate-based electrode material. The substitution of Co^{2+} ions in phosphate framework with Ni^{2+} redox-active ions led to their synergistic interaction with Co^{2+}. These interactions played an important role in enhancing the redox-mediated diffusive charge storage, which led to a significantly higher overall charge storage capability. Capacitive-type surface charge storage was also observed on the $KCo_{1-x}Ni_xPO_4$ electrodes, which confirmed their Hybrid storage behavior.

Among the synthesized compositions, the $KCo_{0.5}Ni_{0.5}PO_4$ proved to have superior electrochemical properties, with a specific capacity of 173 mAh/g and a capacitance of 1038 F/g at a current density of 0.5 A/g. It is due to the near 1:1 Co:Ni composition, that made charge storage efficiency in Hybrid Supercapacitor (HSC) mode very highly effective. The charge storage mechanism predominantly observed was intercalative pseudocapacitive behavior rather than storage based on the surface.

A detailed analysis showed that the charge storage contributions came about 58% from intercalative (bulk) charge storage and 42% from capacitive (surface) storage. The reason for

the predominant intercalative charge storage arose from the active role of Co^{2+}/Co^{3+} and Ni^{2+}/Ni^{3+} redox couples' involvement, which ensured efficient electron transfer with an overall enhancement in energy storage.

The $KCo_{0.5}Ni_{0.5}PO_4$ electrodes also demonstrated superior cycling performance at high current density conditions. At a current density of 5 A/g, the electrodes maintained 88.93% of their initial capacity after 5000 charge-discharge cycles, indicating their excellent stability. The coulombic efficiency ($(\eta = {}^{t_d}/_{t_c})$, where t_d and t_c represent discharge and charge times, respectively) was remarkably high, which further confirmed the reliability of the material in prolonged cycling operations.

For assessing its practical applicability, a full-cell Hybrid Supercapacitor was fabricated using activated carbon as the negative electrode and $KCo_{0.5}Ni_{0.5}PO_4$ as the positive electrode (AC//$KCo_{0.5}Ni_{0.5}PO_4$ cell). The AC//$KCo_{0.5}Ni_{0.5}PO_4$ HSC provided an exceptional energy density of 183.7 Wh/kg with a power density of 414 W/kg in a 2M KOH aqueous electrolyte within a potential window of 1.6 V at a current rate of 0.5 A/g. At the same time, with a high current rate, the device was impressive in a power density of 7952 W/kg and managed to store energy up to 36.4 Wh/kg by its current rate at 10 A/g.

The full cell displayed little degradation even after 5000 cycles. It lost 4.7% coulombic efficiency but remained at a level of 87.2% of the original capacity of $KCo_{0.5}Ni_{0.5}PO_4$, pointing out durability and efficiency for real life application.

In summary, $KCo_{0.5}Ni_{0.5}PO_4$ has very promising electrochemical performance for application as a Hybrid electrode material for Supercapacitors, since its high specific capacity and very high cycling stability, coupled with better power and energy densities, render this a promising candidate for grid-scale applications for energy storage. The environmental-friendly, stable nature of this material further improves prospects of using it in modern high-performance

energy storage systems which shall meet the need of energy storage for efficient supply and consumption of power.

References:

[1] R. Eisenberg, “Addressing the Challenge of Carbon-Free Energy,” *ACS Energy Lett.*, vol. 3, no. 7, pp. 1521–1522, 2018, doi: 10.1021/acsenergylett.8b00889.

[2] S. Chu and A. Majumdar, “Opportunities and challenges for a sustainable energy future,” *Nature*, vol. 488, no. 7411, pp. 294–303, 2012, doi: 10.1038/nature11475.

[3] K. Subramanyan, M. L. Divya, and V. Aravindan, “Dual-carbon Na-ion capacitors: progress and future prospects,” *J. Mater. Chem. A*, vol. 9, no. 15, pp. 9431–9450, 2021, doi: 10.1039/d0ta12099e.

[4] E. Capacitors, “What Are Batteries , Fuel Cells , and Supercapacitors ?,” 2004, doi: 10.1021/cr020730k.

[5] D. Kaufman, K. L. Hudson, and R. Mcclamrock, “and Supercapacitors Begin ?,” vol. 343, no. March, pp. 1210–1212, 2014.

[6] J. Liu, C. Xu, Z. Chen, S. Ni, and Z. X. Shen, “Progress in aqueous rechargeable batteries,” *Green Energy Environ.*, vol. 3, no. 1, pp. 20–41, 2018, doi: 10.1016/j.gee.2017.10.001.

[7] J. Cherusseri, D. Pandey, and J. Thomas, “Symmetric, Asymmetric, and Battery-Type Supercapacitors Using Two-Dimensional Nanomaterials and Composites,” *Batter. Supercaps*, vol. 3, no. 9, pp. 860–875, 2020, doi: 10.1002/batt.201900230.

[8] J. B. Goodenough and P. Singh, “Review-Solid electrolytes in rechargeable electrochemical cells,” *J. Electrochem. Soc.*, vol. 162, no. 14, pp. A2387–A2392, 2015, doi: 10.1149/2.0021514jes.

[9] J. Ding, W. Hu, E. Paek, and D. Mitlin, “Review of Hybrid Ion Capacitors : From Aqueous to Lithium to Sodium,” 2018, doi: 10.1021/acs.chemrev.8b00116.

[10] G. Z. Chen, “Understanding supercapacitors based on nano-hybrid materials with interfacial conjugation,” *Prog. Nat. Sci. Mater. Int.*, vol. 23, no. 3, pp. 245–255, 2013, doi: 10.1016/j.pnsc.2013.04.001.

[11] N. Priyadharsini, S. Surendran, B. Senthilkumar, L. Vasylechko, and R. K. Selvan, “Synthesis and Electrochemical Performances of γ-KCoPO4 Nanocrystals as

Promising Electrode for Aqueous Supercapatteries," *ChemElectroChem*, vol. 6, no. 2, pp. 369–377, 2019, doi: 10.1002/celc.201801440.

[12] Y. Jiang *et al.*, "Transition metal oxides for high performance sodium ion battery anodes," *Nano Energy*, vol. 5, pp. 60–66, 2014, doi: 10.1016/j.nanoen.2014.02.002.

[13] P. Singh, K. Shiva, H. Celio, and J. B. Goodenough, "Eldfellite, NaFe(SO4)2: an intercalation cathode host for low-cost Na-ion batteries," *Energy Environ. Sci.*, vol. 8, no. 10, pp. 3000–3005, 2015, doi: 10.1039/c5ee02274f.

[14] L. Sharma and A. Manthiram, "Polyanionic insertion hosts for aqueous rechargeable batteries," *J. Mater. Chem. A*, vol. 10, no. 12, pp. 6376–6396, 2022, doi: 10.1039/d1ta11080b.

[15] M. Singh, S. Kumar, R. Mondal, P. Singh, R. Prakash, and N. Sharma, "Combustion-Synthesized KNiPO4: A Non-toxic, Robust, Intercalating Battery-Type Pseudocapacitive Electrode for Hybrid Supercapacitors as a Large-Scale Energy Storage Solution," *Energy and Fuels*, vol. 37, no. 5, pp. 4094–4105, 2023, doi: 10.1021/acs.energyfuels.2c04092.

[16] M. Minakshi, D. Meyrick, and D. Appadoo, "不同锂配比Li_Ni_1_3_Co_1_3_省略_n_1_3_O_2正极材料的合.pdf," 2013.

[17] A. Agarwal, S. Majumder, and B. R. Sankapal, "Carbon Nanotube-Functionalized Surface-Assisted Growth of Cobalt Phosphate Nanodots: A Highly Stable and Bendable All-Solid-State Symmetric Supercapacitor," *Energy and Fuels*, vol. 36, no. 11, pp. 5953–5964, 2022, doi: 10.1021/acs.energyfuels.2c00600.

[18] H. Li, H. Yu, J. Zhai, L. Sun, H. Yang, and S. Xie, "Self-assembled 3D cobalt phosphate octahydrate architecture for supercapacitor electrodes," *Mater. Lett.*, vol.

152, pp. 25–28, 2015, doi: 10.1016/j.matlet.2015.03.053.

[19] J. Seok, T. Hoai, T. Luu, and Y. H. Lee, “Author ’ s Accepted Manuscript,” *Energy Storage Mater.*, 2017, doi: 10.1016/j.ensm.2017.12.009.

[20] P. K. Katkar, S. J. Marje, S. S. Pujari, S. A. Khalate, A. C. Lokhande, and U. M. Patil, “Enhanced Energy Density of All-Solid-State Asymmetric Supercapacitors Based on Morphologically Tuned Hydrous Cobalt Phosphate Electrode as Cathode Material,” *ACS Sustain. Chem. Eng.*, vol. 7, no. 13, pp. 11205–11218, 2019, doi: 10.1021/acssuschemeng.9b00504.

[21] B. Senthilkumar, Z. Khan, S. Park, K. Kim, H. Ko, and Y. Kim, “Highly porous graphitic carbon and Ni2P2O7 for a high performance aqueous hybrid supercapacitor,” *J. Mater. Chem. A*, vol. 3, no. 43, pp. 21553–21561, 2015, doi: 10.1039/c5ta04737d.

[22] C. Chen *et al.*, “Polypyrrole-Modified NH4NiPO4·H2O Nanoplate Arrays on Ni Foam for Efficient Electrode in Electrochemical Capacitors,” *ACS Sustain. Chem. Eng.*, vol. 4, no. 10, pp. 5578–5584, 2016, doi: 10.1021/acssuschemeng.6b01347.

[23] M. Minakshi Sundaram and D. R. G. Mitchell, “Dispersion of Ni2+ ions: Via acetate precursor in the preparation of NaNiPO4 nanoparticles: Effect of acetate vs. nitrate on the capacitive energy storage properties,” *Dalt. Trans.*, vol. 46, no. 40, pp. 13704–13713, 2017, doi: 10.1039/c7dt02444d.

[24] B. Liang *et al.*, “Controllable Fabrication and Tuned Electrochemical Performance of Potassium Co-Ni Phosphate Microplates as Electrodes in Supercapacitors,” *ACS Appl. Mater. Interfaces*, vol. 10, no. 4, pp. 3506–3514, 2018, doi: 10.1021/acsami.7b14552.

[25] X. Liu *et al.*, “Ni-Doped Cobalt-Cobalt Nitride Heterostructure Arrays for High-Power Supercapacitors,” *ACS Energy Lett.*, vol. 3, no. 10, pp. 2462–2469, 2018, doi: 10.1021/acsenergylett.8b01393.

[26] M. Yang *et al.*, “Effect of nickel doping on the structure, morphology and oxygen

evolution reaction performance of Cu-BTC derived CuCoO2," *Dalt. Trans.*, vol. 51, no. 22, pp. 8757–8765, 2022, doi: 10.1039/d2dt00970f.

[27] Y. Liu, Z. Li, Y. You, X. Zheng, and J. Wen, "Synthesis of different structured FePO4 for the enhanced conversion of methyl cellulose to 5-hydroxymethylfurfural," *RSC Adv.*, vol. 7, no. 81, pp. 51281–51289, 2017, doi: 10.1039/c7ra09186a.

[28] S. Vivekanandhan, M. Venkateswarlu, and N. Satyanarayana, "Ammonium carboxylates assisted combustion process for the synthesis of nanocrystalline LiCoO2 powders," *Mater. Chem. Phys.*, vol. 109, no. 2–3, pp. 241–248, 2008, doi: 10.1016/j.matchemphys.2007.11.027.

[29] Gangulibabu, D. Bhuvaneswari, N. Kalaiselvi, N. Jayaprakash, and P. Periasamy, "CAM sol-gel synthesized LiMPO4 (M=Co, Ni) cathodes for rechargeable lithium batteries," *J. Sol-Gel Sci. Technol.*, vol. 49, no. 2, pp. 137–144, 2009, doi: 10.1007/s10971-008-1870-5.

[30] N. K. Mishra, R. Mondal, T. Maiyalagan, and P. Singh, "Synthesis, Characterizations, and Electrochemical Performances of Highly Porous, Anhydrous Co0.5Ni0.5C2O4for Pseudocapacitive Energy Storage Applications," *ACS Omega*, vol. 7, no. 2, pp. 1975–1987, 2022, doi: 10.1021/acsomega.1c05356.

[31] C. Schlumberger and M. Thommes, "Characterization of Hierarchically Ordered Porous Materials by Physisorption and Mercury Porosimetry—A Tutorial Review," *Adv. Mater. Interfaces*, vol. 8, no. 4, 2021, doi: 10.1002/admi.202002181.

[32] J. Wen *et al.*, "Constructing Multifunctional Metallic Ni Interface Layers in the g-C3N4 Nanosheets/Amorphous NiS Heterojunctions for Efficient Photocatalytic H2 Generation," *ACS Appl. Mater. Interfaces*, vol. 9, no. 16, pp. 14031–14042, 2017, doi: 10.1021/acsami.7b02701.

[33] A. Mukhtar, N. Mellon, S. Saqib, S. P. Lee, and M. A. Bustam, "Extension of BET

theory to CO2 adsorption isotherms for ultra-microporosity of covalent organic polymers," *SN Appl. Sci.*, vol. 2, no. 7, pp. 1–4, 2020, doi: 10.1007/s42452-020-2968-9.

[34] G. Wang, Z. Yan, N. Wang, M. Xiang, and Z. Xu, "NiO/Ni Metal-Organic Framework Nanostructures for Asymmetric Supercapacitors," *ACS Appl. Nano Mater.*, vol. 4, no. 9, pp. 9034–9043, 2021, doi: 10.1021/acsanm.1c01628.

[35] N. K. Mishra, A. K. Singh, R. Mondal, and P. Singh, "NiC2O4 · 2H2O Nanoflakes: A Novel Redox-mediated Intercalative Pseudocapacitive Electrode for Supercapacitor Applications in Aqueous KOH and Neutral Na2SO4 electrolytes," *ChemistrySelect*, vol. 7, no. 21, 2022, doi: 10.1002/slct.202201134.

[36] N. K. Mishra, R. Mondal, and P. Singh, "Synthesis, characterizations and electrochemical performances of anhydrous CoC2O4nanorods for pseudocapacitive energy storage applications," *RSC Adv.*, vol. 11, no. 54, pp. 33926–33937, 2021, doi: 10.1039/d1ra05180f.

[37] R. Sahoo *et al.*, "Redox-Driven Route for Widening Voltage Window in Asymmetric Supercapacitor," 2018, doi: 10.1021/acsnano.8b04040.

[38] N. R. Chodankar *et al.*, "True Meaning of Pseudocapacitors and Their Performance Metrics: Asymmetric versus Hybrid Supercapacitors," *Small*, vol. 16, no. 37, pp. 1–35, 2020, doi: 10.1002/smll.202002806.

[39] N. B. Velhal *et al.*, "Exploring the Effect of Ultrafast Intensive Pulsed Light (IPL) Annealing on the Structure and Performance of Cobalt Oxide Electrodes for Supercapacitors," *ACS Appl. Energy Mater.*, vol. 6, no. 14, pp. 7405–7418, 2023, doi: 10.1021/acsaem.3c00656.

[40] S. Rudra *et al.*, "Redox-Guided Synthesis of Au-V2O5-MnO2 Nanoflower Composites

with Enhanced Electrical Conductance for Supercapacitor Applications," *ACS Appl. Nano Mater.*, vol. 6, no. 3, pp. 1648–1659, 2023, doi: 10.1021/acsanm.2c04584.

[41] S. Sathishkumar *et al.*, "Bimetal Pyrophosphate of CoNiP2O7@polypyrrole Nanocomposite- Based Electrode for Hybrid Supercapacitor Applications," *Energy Technol.*, vol. 2301589, pp. 1–12, 2024, doi: 10.1002/ente.202301589.

[42] P. Matheswaran, P. Karuppiah, S. M. Chen, and P. Thangavelu, "A binder-free Ni2P2O7/Co2P2O7nanograss array as an efficient cathode for supercapacitors," *New J. Chem.*, vol. 44, no. 30, pp. 13131–13140, 2020, doi: 10.1039/d0nj00890g.

[43] M. Z. Iqbal *et al.*, "Copper doped cobalt-manganese phosphate ternary composites for high-performance supercapattery devices," *J. Energy Storage*, vol. 35, no. November 2020, p. 102307, 2021, doi: 10.1016/j.est.2021.102307.